Fulfillment of the kinetic Bohm criterion in a quasineutral particle-in-cell model

Eduardo Ahedo,[1,a)] Robert Santos,[1] and Félix I. Parra[2]
[1]*Universidad Politécnica de Madrid, Madrid 28040, Spain*
[2]*Rudolf Peierls Centre for Theoretical Physics, University of Oxford, Oxford OX1 3NP, United Kingdom*

(Received 13 January 2010; accepted 28 May 2010; published online 21 July 2010)

Quasineutral particle-in-cell models of ions must fulfill the kinetic Bohm criterion, in its inequality form, at the domain boundary in order to match correctly with solutions of the Debye sheaths tied to the walls. The simple, fluid form of the Bohm criterion is shown to be a bad approximation of the exact, kinetic form when the ion velocity distribution function has a significant dispersion and involves different charge numbers. The fulfillment of the Bohm criterion is measured by a weighting algorithm at the boundary, but linear weighting algorithms have difficulties to reproduce the nonlinear behavior around the sheath edge. A surface weighting algorithm with an extended temporal weighting is proposed and shown to behave better than the standard volumetric weighting. Still, this must be supplemented by a forcing algorithm of the kinetic Bohm criterion. This postulates a small potential fall in a supplementary, thin, transition layer. The electron-wall interaction is shown to be of little relevance in the fulfillment of the Bohm criterion. © *2010 American Institute of Physics*. [doi:10.1063/1.3456516]

I. INTRODUCTION

The application of a two-scale asymptotic analysis to a small-Debye length plasma separates the study of the bulk quasineutral plasma from the thin Debye sheath adjacent to the wall. Furthermore, under rather general conditions, that sheath is quasiplanar, quasisteady, collisionless, and unmagnetized. Then, the sheath existence requires the fulfillment of the Bohm criterion (BC) at the sheath edge.[1–4] For the common negative (i.e., ion-attracting) sheath, the BC states that the ion flux cannot enter the sheath "subsonically" (in a particular sense to be clarified later). Physically, a subsonic ion flow develops a thin-scale space-charge rippling but not a monotonic space-charge layer. In its simplest formulation, for a plasma constituted by monoenergetic ions of charge number Z and electrons of temperature T_e satisfying the Boltzmann relation, the BC takes the *simple* form

$$M_0 = u_{ni}/c_{s0} \geq 1, \quad c_{s0} = \sqrt{ZT_e/m_i}, \tag{1}$$

where c_{s0} is the cold-ion sound speed, u_{ni} is the ion macroscopic velocity perpendicular to the wall, and M_0 is the plasma Mach number in the fluid equivalence (throughout the paper subindex n will refer to the wall-perpendicular direction). For a general velocity distribution function of (wall-attracted) ions, the exact or *kinetic BC* was formulated by Harrison and Thompson[3] and will be presented later in the paper.

The conditions of the bulk quasineutral plasma determine whether the ion flux reaches sonically or supersonically the sheath edge. For a steady-state plasma, quiescent far from the wall, and without the possibility of a regular (i.e., with finite derivatives) sonic crossing within the bulk region, the sonic form of the BC, $M_0=1$, is the only possible transition at the sheath edge. However, the supersonic BC, $M_0>1$, applies, for instance, (1) for supersonic beams (such as the plume of a plasma thruster discharge) impacting frontally on a floating plate, or (2) at one or the two edges of intermediate double layers.[5–7] In plasma flows with strong, low-frequency oscillations, the supersonic BC is expected to apply intermittently.

In a fluid formulation of the quasineutral plasma, the BC is one boundary condition of the ion differential equations. Then, if the quasineutral solution is subsonic, the ambipolar electric field at the sheath edge tends to infinity in the quasineutral scale. On the contrary, if the ion flow near the sheath edge is supersonic, the ambipolar field remains finite. In both cases, the space-charge electric field at the edge tends to zero in the sheath inner scale. The matching of these disparate asymptotic behaviors takes place in a transition layer of an intermediate scale.[4] In the quasineutral scale, the sheaths are just surface discontinuities. In general, if the BC is satisfied and the sheath existence is assured, the interest is more on the sheath jump conditions (such as the potential fall and the particle and energy fluxes) than on the sheath inner profiles.

Several issues related to the BC fulfillment arise when a quasineutral particle-in-cell (PIC) model[8] is adopted for the ions, the particular formulation used for the (confined) electrons being less relevant. First, there are difficulties for standard linear algorithms on a discrete mesh to reproduce the correct square-root dependence of the electrostatic potential and the plasma density near the boundary of a subsonic quasineutral domain. Second, since ion macroparticles are advanced in time according to the electromagnetic force on them, there is not an immediate way of imposing the BC at the boundary of the quasineutral domain. Third, since ion particles leaving the domain are not returned back (assuming that they recombine into neutrals), there is the question of

a)Electronic mail: eduardo.ahedo@upm.es.

whether the ion flux achieves *by itself* the sonic/supersonic condition at the boundary. Fourth, the PIC ion population is generally far from being monoenergetic and consists often of ions with different charge numbers, which makes, in principle, the simple BC (1) invalid.

The experience shows that for practical sizes of PIC meshes and standard linear algorithms, the ion flux can be far from achieving the BC by itself. This has led researchers to look for practical ways of imposing it. Hutchinson[9] suggested to modify the weighting scheme at the boundary node. Instead of using a linear scheme, he imposed the square-root dependence of the variables between the node at the boundary and the one next to it, with the expectation that the plasma density will follow naturally the electrostatic potential shape. He found the method valid for a collecting sphere in a flowing plasma with Boltzmann electrons. Instead of this nonlinear boundary weighting scheme, Lampe *et al.*[10] proposed to force the fulfillment of the BC by including a thin strip between the quasineutral domain and the Debye sheath, where an incremental perpendicular velocity (positive or negative) is added to all ion particles leaving the PIC domain such that $M_0=1$ is satisfied at the sheath edge. Both Hutchinson and Lampe *et al.* worked with the simple BC in Eq. (1); attempts by Hutchinson to implement the kinetic BC showed it to be too subject to noise to be useful.

This paper deals with the fulfillment of the kinetic BC for a generic velocity distribution function of ions of different charge numbers. Our two main goals are the derivation of a suitable boundary weighting algorithm, more reliable than the standard ones for internal nodes of Birdsall and Langdon,[8] and the implementation within a PIC model of a consistent forcing algorithm of the kinetic BC.

The PIC model used here for these objectives is one designed to study the plasma discharge in a Hall thruster. Fife and Martínez-Sánchez[11,12] developed the first two-dimensional (2D) hybrid model for Hall thrusters, HPHall. Its two main elements are the PIC submodel for heavy species (ions and neutrals) and the anisotropic fluid submodel for magnetized electrons. Macroscopic magnitudes for ions and neutrals are obtained from a standard volumetric weighting (VW).[8] Quasineutrality in the computational domain is satisfied automatically by setting that the plasma density, $n_e(\boldsymbol{r},t)$, is determined by the PIC submodel only. Thus, the boundaries of the PIC computational domain are the edges of the Debye sheaths. The simulation model we use is a much updated version of the original HPHall, with improvements implemented at different phases and reported in Refs. 13–16 among others. HPHall is also the base model upon which other 2D hybrid codes for Hall thrusters have been built.[17–19] In any case, the results of this work should be applicable to ion PIC models of different plasma discharges.

In the first phase of improvements of HPHall, Parra and Ahedo started to analyze the fulfillment of the BC (1) in the ion PIC submodel. First,[20] they showed that the plasma gradients and the value of M_0 at the boundary were very sensitive to the mesh size. Solutions for a typical mesh ("typical" meaning a mesh supposedly fine enough to reproduce internal plasma gradients reliably) had Mach numbers at the boundaries as low as $M_0\sim 0.25$. When the mesh size was refined by a factor of 5 near the radial boundaries (increasing the simulation time by a factor of 20), M_0 increased to about 0.5 and, more important, there were significant changes on the plasma gradients and the plasma fluxes to the wall. Then, they conclude that (i) the use of the VW at the boundaries nodes is inadequate, (ii) local changes near the boundaries modify *nonlocally* the plasma response, and (iii) $M_0\approx 1$ is unattainable with practical meshes and the VW. Later,[21,22] they proposed three alternative boundary weighting schemes: a corrected VW, a surface weighting, and a BC forcing scheme, this last one similar to the method proposed by Lampe *et al.*

In Sec. II of this paper, the three alternative boundary weighting algorithms are evaluated with respect to the fulfillment of the simple BC (1). In Sec. III, the implementation of the kinetic BC in a PIC model is developed and the differences with the simple BC (1) are highlighted. In Sec. IV, the algorithms presented in Sec. II are improved: an extended surface weighting scheme with small numerical noise is proposed and the kinetic BC forcing algorithm is developed. Section V discusses the influence of the electron and wall formulations on the BC fulfillment and the way to deal with "supersonic" Bohm transitions; it ends with conclusions.

II. ASSESSMENT OF BOUNDARY WEIGHTING SCHEMES

The numerical integration of the hybrid model advances the PIC and electron submodels sequentially with a timestep Δt around 10^{-2}–10^{-1} μs.[13] Inputs of the PIC submodel (and outputs of the electron submodel) are the ambipolar electric potential and the electron temperature, $\phi(\boldsymbol{r},t)$ and $T_e(\boldsymbol{r},t)$. Outputs of the PIC submodel (and inputs of the electron submodel) are the particle densities and fluxes, n_α and $\boldsymbol{g}_\alpha\equiv n_\alpha \boldsymbol{u}_\alpha$, of each heavy species: neutrals ($\alpha=n$), single ions ($\alpha=i_1$), and double ions ($\alpha=i_2$). Plasma quasineutrality yields the electron (or plasma) density, $n_e=n_{i_1}+2n_{i_2}$, as input of the electron submodel.

Figure 1(a) sketches the axisymmetric simulation domain, the PIC mesh, and the thruster elements. The cathode line is the magnetic line intersecting the cathode/neutralizer. A discharge potential V_d is applied between a point at the cathode line and the metallic anode. The anode drives a discharge current I_d between the plasma and the external circuit. Thus, the discharge current is also the electron current injected at the cathode line. The ambipolar electric field splits this current into an outward beam, which makes the plasma plume beyond the cathode line current-free, and an inward beam, used to ionize the gas injected at the back of the chamber and to provide quasineutrality. The lateral walls of the chamber are made of a ceramic material with a high secondary-electron-emission (SEE) yield, characterized mainly by the electron temperature T_1 leading to a 100% yield ($T_1\simeq 26.4$ eV in the simulations here).

Figure 1(b) depicts the magnetic lines created by the *external* magnetic circuit that surrounds the chamber (the plasma-induced magnetic field is negligible). These lines are part of the mesh used to integrate the anisotropic fluid equa-

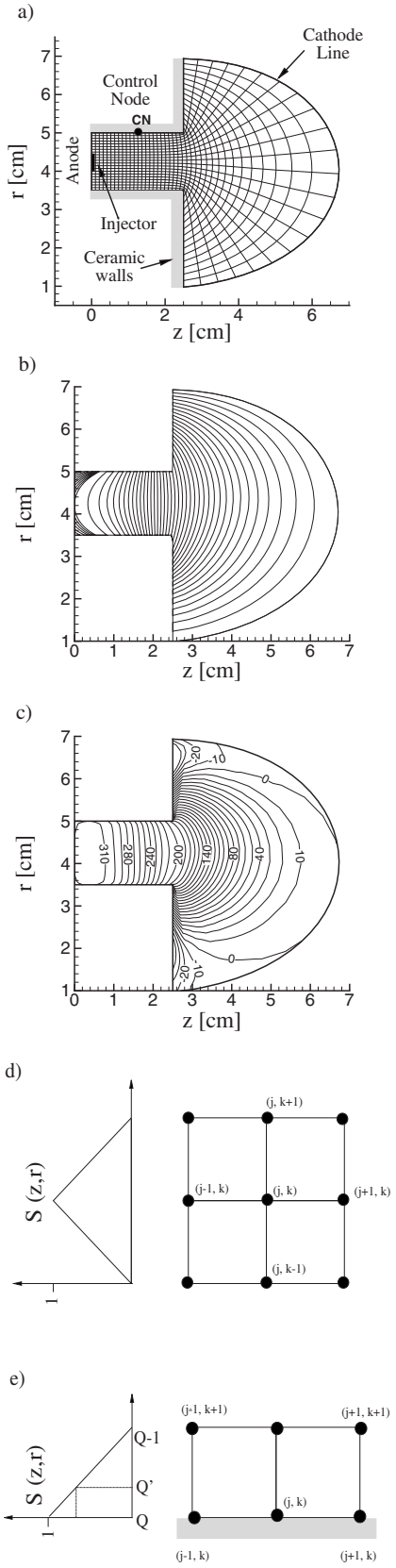

FIG. 1. (a) Sketch of the PIC domain and mesh. The back surface is the metallic anode and part of it is the gas injector. The lateral surfaces are made of a dielectric material. The cathode line is the magnetic line intersecting the cathode/neutralizer. CN is a control node to measure instant values of plasma magnitudes. (b) Magnetic field lines generated by the external magnetic circuit. (c) Lines of constant ambipolar electric potential for a typical simulation with V_d=300 V. [(d)–(e)] Sketch of the region of influence of internal and boundary nodes, respectively, for the VW.

tions of the electron submodel. Just as an illustration, Fig. 1(c) plots, for a typical simulation, equipotential lines of the time-averaged ambipolar electric field. The deviation between the equipotential and magnetic lines is explained by the Boltzmann relation along the magnetic lines.

In order to compare the results for different weighting schemes and BC expressions, most results here are for a unique operational point and a unique mesh. The typical simulation time is $O(10^4\Delta t)\sim O(1\ \text{ms})$. The thruster operates with a discharge voltage of 300 V between anode and cathode, an injected mass flow of xenon at the back of the chamber of 5 mg/s, and a maximum magnetic field (near the chamber exit) of 250 G. The mesh consists of $O(10^3)$ cells and about 30 particles per cell and heavy species. This relatively low number of particles is aimed at emphasizing the issues under discussion here. In order to evaluate the relevance of double ions in the fulfillment of the BC, two different simulations are run: *simulation 1* and *simulation 2* with the source term for double ions switched off and on, respectively.

At the internal nodes, the macroscopic magnitudes for the heavy species are obtained from a standard, first-order, VW based on the three properties of the macroparticles: their velocity $\boldsymbol{v}_p$, charge number Z_p, and number of atoms N_p they represent. Thus, the ion density and the ion current density satisfy[8]

$$n_i|_{\text{VW}} = \frac{1}{\Delta V}\sum_p S(z_p,r_p)N_p,$$

$$\boldsymbol{j}_i|_{\text{VW}} = \frac{e}{\Delta V}\sum_p S(z_p,r_p)N_pZ_p\boldsymbol{v}_p, \tag{2}$$

where $S(z_p,r_p)$ is a bilinear weighting function [Fig. 1(d)], $\Delta V=\int\int_{S>0}2\pi r dr dz S(r,z)$ is the weighted volume of the region of influence of the node (which takes into account cylindrical effects), and the summation applies to all particles in the region of influence.

Boundary weighting algorithms are discussed next. All results in this section are for simulation 1 and the simple BC (1). Figures 2(a)–2(d) compare *time-averaged* results with the different weighting schemes. Figure 2(a) plots the plasma density at an almost radial magnetic streamline, located near the chamber exit; since electrons follow the Boltzmann relation along a magnetic line, the variation of ϕ is $\propto T_e \ln n_e$. Figures 2(b)–2(d) plot n_e and M_0 along the outer dielectric wall of the thruster. The arc variable s is defined along the outer wall in the meridian plane, with intervals $0<s(\text{mm})<25$ and $25<s(\text{mm})$ corresponding to regions inside and outside the chamber (i.e., near plume), respectively.

A. Corrected volumetric weighting

HPHall (Ref. 12) used the algorithm of Eq. (2) at the boundary nodes, limiting the volume of influence to the internal half-side [Fig. 1(e)]. This asymmetric weighting underestimates (overestimates) magnitudes that increase (decrease) toward the boundary. The error is proportional to the cell length in the wall perpendicular direction, ΔL_n, and is

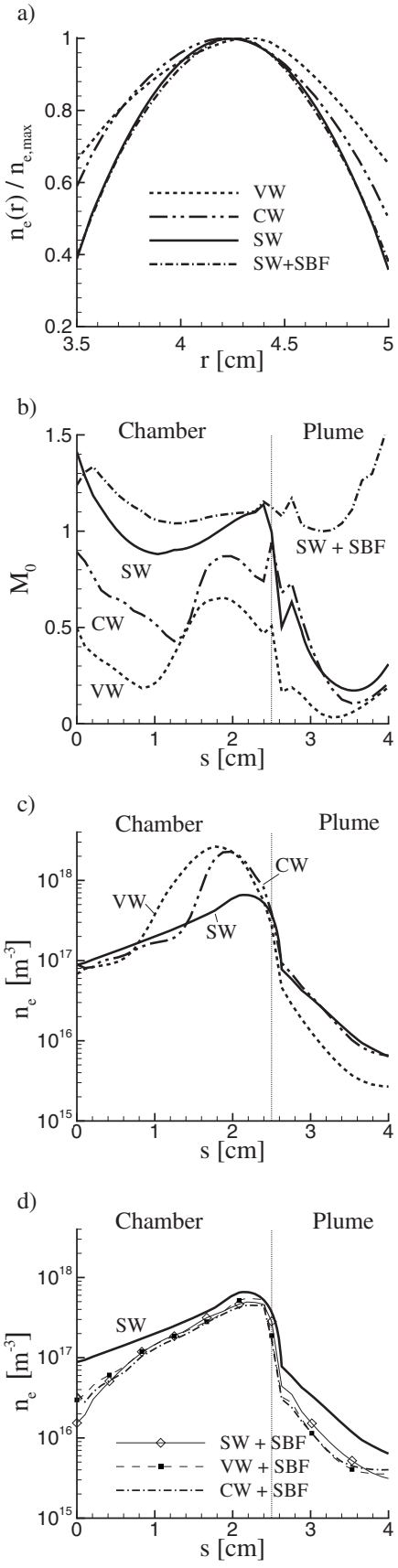

FIG. 2. Time-averaged results for different boundary-weighting schemes. (a) Radial profile of the relative plasma density at a near-radial magnetic streamline, located at $z \simeq 18.5$ mm; n_{max} is the maximum density in that magnetic line. (b) Mach number at the sheath edge along the outer wall. [(c) and (d)] Plasma density along the outer wall. Results are for simulation 1 (without double ions).

large for magnitudes that present large gradients near the sheath boundary, which is the case of ϕ and n_e.

Parra and Ahedo[21] pointed out that, at a boundary node, Eq. (2) yields plasma magnitudes representative of the "center of mass" Q' of that half-volume instead of the boundary [Fig. 1(e)]. For a linear weighting, that center of mass is located at $\boldsymbol{x}_{Q'}=(2\boldsymbol{x}_Q+\boldsymbol{x}_{Q-1})/3$. Hence, the corrected volumetric weighting (CW) at a boundary node is an extrapolation of the weighted values at the location $\boldsymbol{x}_{Q'}$ and the previous node (say, $Q-1$)

$$\chi|_{\mathrm{CW},Q}=\tfrac{3}{2}\chi|_{\mathrm{VW},Q'}-\tfrac{1}{2}\chi|_{\mathrm{VW},Q-1}, \tag{3}$$

with χ a generic plasma magnitude. The CW makes the error proportional to ΔL_n^2. The comparison of the VW and the CW in Figs. 2(a) and 2(b) show that the CW yields larger radial gradients of the plasma density and the electric potential in the bulk of the plasma and a higher M_0 at the sheath edge, but still the BC (1) is far from being satisfied.

B. Surface weighting

Parra *et al.*[22,23] suggested that measuring the properties of the particles crossing (the panel of influence of) a boundary node is more reliable than weighting on the particles staying in its volume of influence. A SW algorithm acts only on particles actually leaving the domain and is not affected by the distortion caused by the one-side VW. The SW for the ion density and current, at a generic boundary node, yields

$$n_i|_{\mathrm{SW}}=\frac{1}{\Delta t\Delta A}\sum_p S(s_p)\frac{N_p}{v_{np}},$$
$$\boldsymbol{j}_i|_{\mathrm{SW}}=\frac{e}{\Delta t\Delta A}\sum_p S(s_p)\frac{N_p}{v_{np}}Z_p\boldsymbol{v}_p, \tag{4}$$

where the summation applies to particles crossing the surface of influence of the node within the timestep Δt, v_{np} is the particle perpendicular velocity, ΔA is the weighted area of the region of influence, and $S(s_p)$ is the weighting function with variable s along the wall. Here, a zeroth-order weighting function, $S(s_p)=1$, has been found satisfactory; a first-order weighting requires the additional cost of computing the location where particles left the domain.

Figures 2(a) and 2(b) show that the SW leads to a further development of the radial plasma structure and a higher M_0 than the CW. In fact, the SW fulfills the BC (1) inside the chamber. The sequence of behaviors of the VW, CW, and SW indicates, first, a direct relation between the development of the radial structure and the increase of M_0 at the sheath edge. Therefore, the fulfillment of the BC is crucial not only for a correct transition to the sheath but also for a correct solution within the quasineutral domain. Second, the SW stands as the best boundary weighting scheme. Nonetheless, the wall regions (like in the plume) with $M_0<1$, the differences among the different weighting schemes in Fig. 2(c) on the time-averaged profiles of n_e, and the large-amplitude noise of the SW scheme commented next, make advisable some refinement of this boundary weighting scheme.

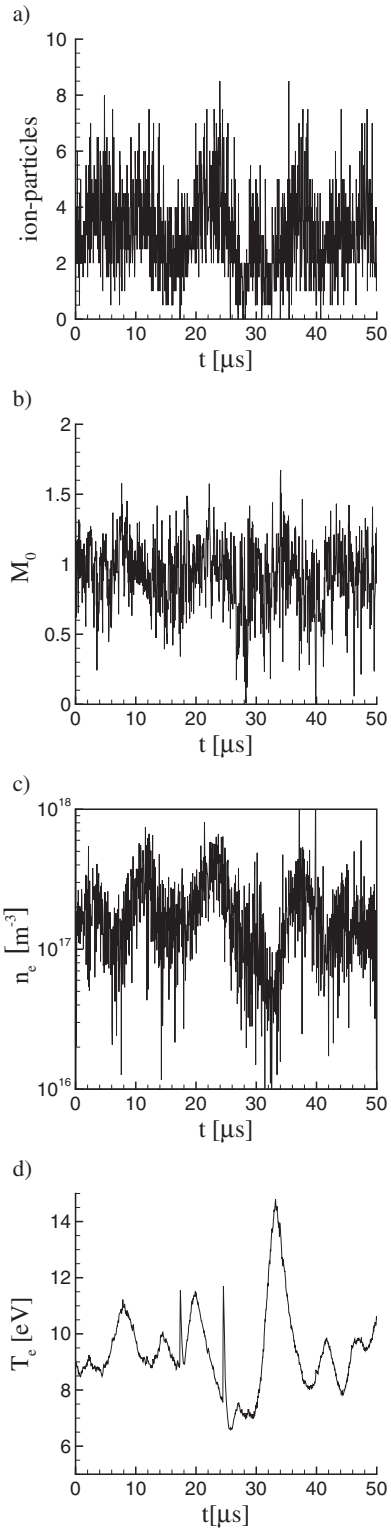

FIG. 3. Instant values at the control node using the surface-weighting scheme. (a) Number of ion particles crossing the node in 1000 timesteps (50 μs). [(b)–(d)] Plasma density, Mach number, and electron temperature for the same temporal sequence. Results are for simulation 1.

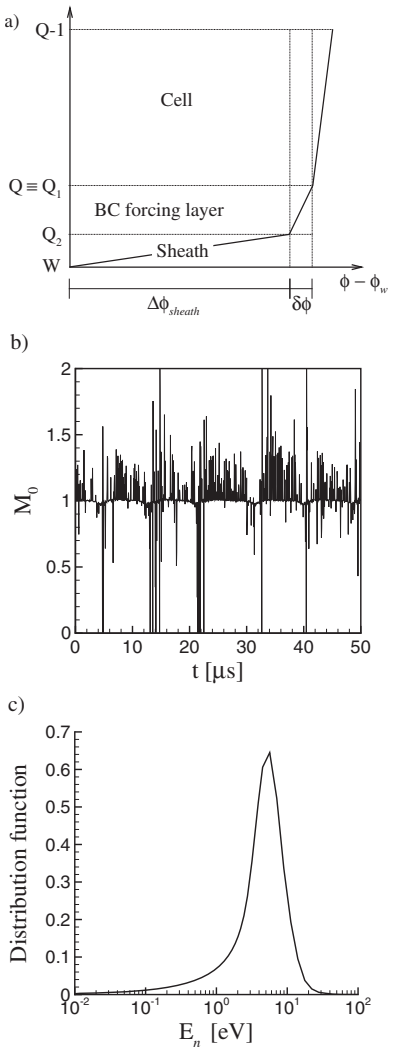

FIG. 4. (a) Sketch of the quasineutral transition layer in the BC forcing scheme. (b) Instant values at the control node of the Mach number when the simple BC forcing scheme is added to the SW. (c) Normalized ion distribution function vs the particle perpendicular energy E_n at the control node.

The numerical noise associated with the SW is illustrated in Fig. 3. Figure 3(a) plots the number of ion particles (each one with its own N_p) crossing the control node—marked in Fig. 1(a)—along 1000 timesteps. The number of crossing particles in one timestep is small and presents a large dispersion. This leads to strong temporal oscillations of n_e and M_0, shown in Figs. 3(b) and 3(c), and these distort the time-averaged values of plasma magnitudes since extreme, nonphysical values have too much weight when time-averaging. Figure 3(d) plots the temporal evolution of T_e at the control node, obtained from the electron fluid submodel. The fluctuations of T_e correspond to the physical transit-time instability[24] and show almost no traces of the high-frequency activity of the PIC results, confirming that the high-frequency oscillations of n_e are basically numerical noise. (The comparison of the oscillations of the fluid and PIC submodels, in order to identify better what is numerical noise, could be an advantage of hybrid models over fully PIC ones.)

C. Forcing of the simple Bohm criterion

Lampe *et al.*[10] proposed to force the fulfillment of the BC. They postulated a thin layer adjacent to the Debye sheath where ion-particle velocities are laid down to determine the average ion flow speed normal to the surface, u_{ni}.

Then, the increment $\delta u_{ni}=c_{s0}-u_{ni}$, *whether positive or negative*, is added to all ion velocities in the strip, such as to bring M_0 to 1. The BC is thereafter self-sustaining with the increment δu_{ni} a small adjustment at each timestep.

Ahedo and Parra[21] proposed a similar BC forcing algorithm. Their idea stems from the fact that a linear weighting scheme on a finite-size mesh is unable to reproduce the local nonlinearity of the electric potential near the sheath edge for a subsonic flow. Consequently, ion particles gain a lower perpendicular energy than they should get in order to fulfill the BC. Their simple Bohm criterion forcing (SBF) algorithm postulates also a thin *BC forcing layer* [Q_1Q_2 in Fig. 4(a)] between the quasineutral PIC domain and the Debye sheath, characterized by the potential fall,

$$\delta\phi=\phi_{Q_1}-\phi_{Q_2}\geq 0, \tag{5}$$

needed to bring the ion flux from $M_{0,Q_1}<1$ to $M_{0,Q_2}=1$. The combination of the potential falls in the thin BC forcing layer and the adjacent PIC cell attempts to both provide the correct perpendicular energy and model the nonlinear behavior near the sheath edge.

In order to be consistent with the spatial scaling hierarchy, the thickness of the BC forcing layer, ℓ_{BF}, must satisfy $\lambda_d\ll\ell_{\mathrm{BF}}\ll\{L_n,\lambda_{\mathrm{col}}\}$ with λ_{col} as the shortest of the collisional mean-free-paths. In particular, there is no plasma production in that layer so that $g_{nQ_1}=g_{nQ_2}$. Then, assuming, as in Eq. (1), that ion particles are monoenergetic, the potential fall in the BC forcing layer is

$$\delta\phi=\min\left\{\frac{T_e}{2e}(1-M_{0,Q_1}^2),\delta\phi_{\max}\right\}, \tag{6}$$

where the provision of a $\delta\phi_{\max}$ is a numerical artifact, meant to avoid too large gradients near the boundary. Thus, the plasma density at the sheath edge Q_2 is

$$n_{eQ_2}=g_{nQ_1}\left(u_{nQ_1}^2+\frac{2e\,\delta\phi}{m_i}\right)^{-1/2}. \tag{7}$$

This density is the one provided by the SBF algorithm to the electron submodel and is used to compute the subsequent profile of ϕ.

A central characteristic of the SBF algorithm is that it is *supplementary* to a primary boundary weighting scheme that determines u_{ni} and the other macroscopic magnitudes at Q_1. Figure 4(b) plots M_0 at the control node when the SBF is supplemented to the SW: instants with $M_0<1$ correspond to $\delta\phi=\delta\phi_{\max}$ in Eq. (6). Although the oscillations of $M_0(t)$ have been reduced greatly, those of $n_e(t)$ are similar to those shown in Fig. 3(c). Figure 4(c) plots, at the control node, the ion distribution function $f_i(E_n)$, with $E_n=m_iv_{npQ_1}^2/2$, which has been obtained from all particles crossing the node in the whole simulated time (and weighted each particle with its N_p). The average perpendicular energy of ions is 6.0 eV and the plasma temperature is about 9.2 eV. This agrees well with the simple estimate $E_n\sim T_e/2$ for a collisionless presheath.

Our SBF algorithm differs from the one of Lampe *et al.* in two important features. The first one is that we admit the inequality form of the BC, $M_{0,Q_2}\geq 1$, so that the SBF is not applied when $M_{0,Q_1}>1$. On the contrary, Lampe *et al.* implemented the restrictive form $M_{0,Q_2}=1$ so that ions are slowed down when $M_{0,Q_1}>1$. This subject will be discussed in Sec. IV B. The second and main difference is that our SBF algorithm is energy-conserving since the same energy, $e\,\delta\phi$ (instead of the same perpendicular velocity, δu_{ni}) is supplemented to all particles in the BC forcing layer. Of course, both BC forcing algorithms would yield identical results if the ion particles were monoenergetic (and $M_{0,Q_1}<1$ at every instant). However, if the ion velocity distribution function presents a large dispersion, the application of the SBF algorithm would be justified only if the resulting $\delta\phi$ (or δu_{ni}) is almost independent of the distribution function, which is not correct as we show in Sec. III. Figure 4(c) confirms that $f_i(E_n)$ has indeed a significant velocity dispersion.

The effect of applying the SBF to the three weighting schemes (VW, CW, and SW) is illustrated in Fig. 2(d), which plots time-averaged profiles of the plasma density along the sheath edge of the outer wall. Observe, first, the excellent convergence of results of the three primary weighting schemes when the SBF is supplemented, in spite of their significant differences in Fig. 2(c). Second, the SW is, among the primary weighting schemes, the closer one to the SBF-supplemented schemes. The trends shown in Fig. 2(a) and the convergence illustrated in Fig. 2(d) lead us to conclude the SW supplemented with the SBF is the best choice (for the simple BC). An additional reason to select the SW as primary weighting scheme is that its matching with a BC forcing scheme is more physical: the incremental potential fall at the BC forcing layer is more naturally applied to the particles leaving the domain on the SW scheme than to the last cell particles weighted on the CW scheme.

III. THE KINETIC BOHM CRITERION

The electrostatic potential in a thin, collisionless sheath satisfies the Poisson's equation

$$\frac{d^2\phi}{dz^2}=-\frac{e}{\epsilon_0}\sum_s Z_sn_s(\phi), \tag{8}$$

where subindex s stands for the different species of a multicomponent plasma and Z_s for its charge number. The BC at the sheath edge Q is

$$\sum_s Z_s\left.\frac{dn_s}{d\phi}\right|_Q\leq 0, \tag{9}$$

and stems from imposing that the non-neutral solution of Poisson's equation that starts from Q corresponds to a locally monotonic potential (i.e., it dismisses oscillatory solutions).[3,4]

For a negative sheath, the BC (9) becomes

$$P\equiv\frac{1}{T_e}\sum_j Z_jn_j-\sum_j\frac{Z_j}{e}\frac{dn_j}{d\phi}\geq 0, \tag{10}$$

where the summation index j stands only for the various ions species, the subindex Q for the sheath edge has being omitted, plasma quasineutrality at the sheath edge, $n_{eQ}=\Sigma_jZ_jn_{jQ}$,

has been applied, T_e is the effective electron temperature, defined as

$$T_e = [n_e e d\phi/dn_e]_Q, \tag{11}$$

and the "Bohm function" P is defined for later convenience.

The expressions of $n_j(\phi)$ in Eq. (10) depend on the type of formulation used for ions. The general, kinetic formulation yields

$$n_i = \sum_j n_j = \sum_j \int_0^\infty dv_n f_j(v_n), \tag{12}$$

with $f_j(v_n)$ as the velocity distribution function of species j at the sheath edge Q in terms of the perpendicular velocity, once the moments over the two other velocity components have been taken. Then, Eq. (10) becomes the kinetic BC (Ref. 3)

$$P \equiv \sum_j \int_0^\infty dv_n f_j(v_n)\left(\frac{Z_j}{T_e} - \frac{Z_j^2}{m_i v_n^2}\right) \geq 0. \tag{13}$$

Clearly, the PIC-SW version of this kinetic BC is

$$P \equiv \frac{1}{\Delta t \Delta A}\sum_p \frac{N_p}{v_{np}}\left(\frac{Z_p}{T_e} - \frac{Z_p^2}{m_i v_{np}^2}\right) \geq 0. \tag{14}$$

Let $\langle\chi\rangle = n_i^{-1}\Sigma_j \int_0^\infty dv_n f_j(v_n)\chi(v_n)$ and $\langle\chi\rangle = (n_i \Delta t \Delta A)^{-1} \times \Sigma_p N_p v_{np}^{-1}\chi_p$ be the average value of a generic magnitude χ in the kinetic and PIC formulations, respectively. The best parameter both to evaluate the fulfillment of the kinetic BC and to compare with the simple BC is the "Mach–Bohm" number

$$M_k = \tilde{u}_{ni}/c_{s0}, \tag{15}$$

with

$$\tilde{u}_{ni} = \frac{\langle Z\rangle}{\sqrt{\langle Z^2 v_n^{-2}\rangle}}, \quad c_{s0} = \sqrt{\frac{\langle Z\rangle T_e}{m_i}}, \tag{16}$$

the relevant velocity of the kinetic BC and the sound speed for cold ions of average charge number $\langle Z\rangle$, respectively. Using M_k the kinetic BC (14) becomes $M_k \geq 1$.

The fluid Mach number is $M_0 = u_{ni}/c_{s0}$, with $u_{ni} = \langle v_n\rangle$ as the velocity of the ion flow. Then, the ratio

$$M_k/M_0 \equiv \tilde{u}_{ni}/u_{ni},$$

measures the difference between the simple and kinetic Bohm criterions and is going to depend largely on the dispersion of the ion velocity distribution function. For instance, ions with $v_n \ll u_{ni}$ (created near the plasma boundary) have a much larger weight in $\tilde{u}_{ni}$ than in u_{ni}. Let $c_n = v_n - u_{ni}$ be the peculiar velocity of an ion (or ion particle). If the dispersion of the ion velocity distribution is small, i.e., $\langle|c_n|\rangle \ll u_{ni}$, and all ions have the same charge number Z, the kinetic BC takes the "warm-fluid" form[4]

$$\frac{Z}{T_e} - \frac{Z^2}{m_i(u_{ni}^2 - 3\langle c_n^2\rangle)} \geq 0, \tag{17}$$

with $m_i\langle c_n^2\rangle$ a kind of ion temperature. Then,

$$M_k \equiv \tilde{u}_{ni}/c_{s0} = u_{ni}/c_s,$$

with $c_s = \sqrt{ZT_e/m_i + \langle c_n^2\rangle}$ as the *actual* sound speed for the warm-ion fluid. Since $c_{s0} < c_s$, one has $\tilde{u}_{ni} < u_{ni}$ and $M_k < M_0$, and the simple BC is a weaker condition than the kinetic BC.

When the velocity dispersion is large, as it happens to f_i in Fig. 4(c), the ratio M_k/M_0 becomes smaller and the one-fluid analogy of Eq. (17) for the kinetic BC is lost (or becomes simply formal). Since $v_n > 0$ for (wall-attracted) ions, a large velocity dispersion, i.e., $\langle|c_n|\rangle \geq O(u_{ni})$, implies that there are particles with $v_n \ll u_{ni}$ [see Fig. 4(c)]. These particles dominate in determining $\tilde{u}_{ni}$ [Eq. (16)] and therefore $\tilde{u}_{ni} \ll u_{ni}$ and $M_k \ll M_0$. This discrepancy between M_k and M_0 and therefore between the simple and the kinetic BCs is illustrated in Figs. 5(a)–5(c), commented below.

Observe that the presence of simple and double ions yields by itself a significant velocity dispersion: double-ion velocities are about $\sqrt{2}$ times higher than simple-ion ones. Indeed, two monoenergetic populations of simple and double ions with velocities u_{ni_1} and u_{ni_2}, constitute a simple and illustrative example of the difference between M_k and M_0. The kinetic BC for that ion distribution is

$$\frac{n_{i_1} + 2n_{i_2}}{T_e} - \frac{n_{i_1}}{m_i u_{ni_1}^2} - \frac{4n_{i_2}}{m_i u_{ni_2}^2} \geq 0, \tag{18}$$

which can be obtained from a multifluid model for ions too.[25] The ratio M_k/M_0 is a simple function of n_{i_2}/n_{i_1} and u_{ni_2}/u_{ni_1}. Clearly, there is no additional insight on interpreting Eq. (18) as a sonic-supersonic condition on a single fluid, i.e., $u_{ni} \geq c_s$ for certain c_s.

IV. BOUNDARY WEIGHTING BASED ON THE KINETIC BOHM CRITERION

Section II concluded that the SW scheme plus a BC forcing algorithm are the best boundary weighting scheme in terms of numerical reliability and physical interpretation, but it presents large numerical oscillations. Section III concluded that, in general, the simple BC is a bad estimate of the kinetic BC and should not be used in a BC forcing algorithm. The solutions to these two issues are tackled next.

A. Extended surface weighting

The main cause for the numerical noise created by the SW is that the number of particles crossing a node in one timestep, Δt, is small and with a large dispersion. The choice of the PIC timestep is based on aiming a low numerical noise on the VW of plasma magnitudes. Thus, the numerical noise at internal nodes is expected to decrease as Δt decreases. On the contrary, low numerical noise of the SW requires a large timestep so that many particles cross each boundary panel within that timestep. In our simulations $\Delta t (\sim 5 \times 10^{-8}$ s) is selected in order that a typical ion takes about two timesteps to cross one cell. A simple estimate yields that the suitable timestep for the zeroth-order SW should be about one-order-of magnitude larger than Δt, in order that the noise levels at boundary and internal nodes be comparable. [Interestingly, Lampe *et al.*, working with PIC models for both ions and electrons and in order to determine the potential fall in the Debye sheath, counted the electrons that reach the wall

(from the high-energy tail of the distribution at the sheath edge) and point out that the counting timestep must be large to avoid noise. However, we do not find any hint in their paper suggesting they are using a SW scheme to compute u_{ni} at the sheath edge.]

A way to satisfy the conflicting volumetric and surface weighting requirements is to use an extended timestep for the surface weighting. In practice, this can be executed with little computational cost if the SW is applied on the particles crossing a boundary node in k timesteps, which is on a time interval $k\Delta t$. This leads to the following extended surface weighting (ESW) algorithm (for n_i):[26]

$$n_i|_{\mathrm{ESW}} = \frac{1}{k\Delta t \Delta A} \sum_k \sum_p \frac{N_p}{v_{np}}, \tag{19}$$

where the summation on k is extended to the last k-timesteps, and we took $S(s_p)=1$. Working with $k \sim O(10)$ instead of $k=1$ increases only slightly the computer memory and time since it affects exclusively to boundary nodes.

Figures 5(a) and 5(b) show the time-averaged values of M_k and M_0, at the outer sheath edge, as k is increased from 1 to 50. The changes with k are attributed to the oscillations on the scale Δt, which fade out as k increases. Observe that $M_k < M_0$ always; for $k=50$ and on average along the outer wall, $M_k \sim 0.56$ and $M_0 \sim 0.99$. The larger sensitivity of M_k to small values of v_n explains that it changes much more with k than M_0. Figures 5(c) and 5(d) plot instant values of M_k, M_0, and n_e at the control node when $k=50$ is used in the ESW. They show, first that M_k/M_0 is rather small at some instants. Second, the comparison with Figs. 3(b) and 3(c) shows that the high-frequency noise has been canceled and only the transit-time oscillation remains. [Indeed, an upper limit of k would be to keep $(k\Delta t)^{-1}$ much higher than the transit-time frequency.]

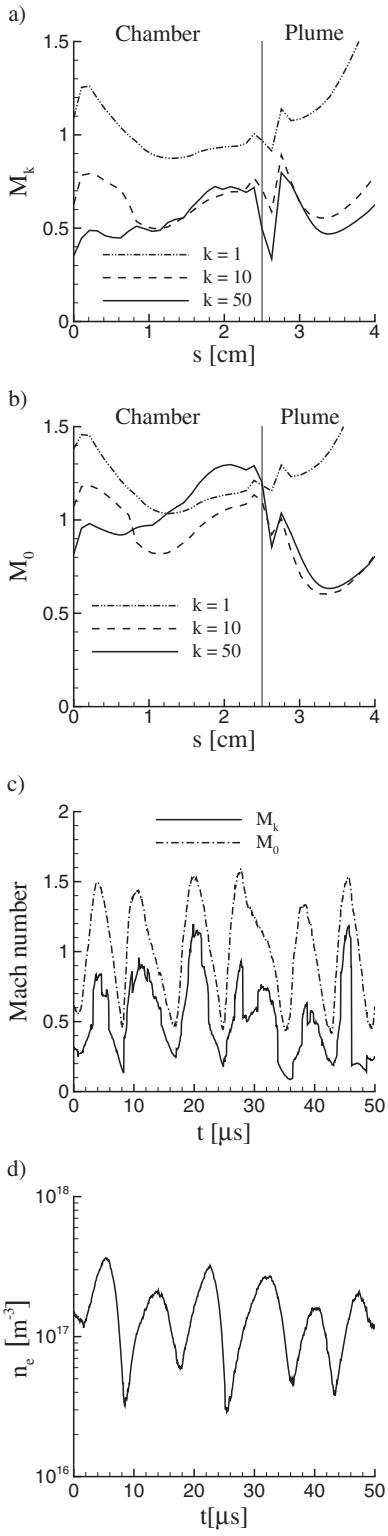

FIG. 5. Results for the ESW and simulation 2. [(a) and (b)] Time-averaged values along the outer wall of the Mach–Bohm number and the Mach number for different values of the timestep number k used by the ESW. [(c) and (d)] Instant values at the control node of three plasma magnitudes for $k=50$.

B. Forcing of the kinetic Bohm criterion

The use of $k=O(10)$ within the ESW algorithm eliminates most of the high-frequency noise but also shows that the kinetic BC is far from being fulfilled in spite of $M_0 \sim 1$. Figure 5(c) shows instants with M_k as low as 0.1. Therefore, the ESW still needs to be supplemented with a forcing algorithm of the kinetic BC.

In the ESW framework, the kinetic BC (14) becomes

$$P \equiv \frac{1}{k\Delta t \Delta A} \sum_k \sum_p \frac{N_p Z_p}{v_{np}} \left(\frac{1}{T_e} - \frac{Z_p}{m_i v_{np}^2} \right) \geq 0. \tag{20}$$

The kinetic BC forcing (KBF) algorithm we propose is the extension of the simple BC forcing algorithm of Sec. II C to a nonmonoenergetic ion distribution. At those instants when P in Eq. (20) is negative, the thin, collisionless BC forcing layer Q_1Q_2 is included, with a potential fall $\delta\phi$ [Eq. (5)]. The potential fall must bring $P_{Q_1} < 0$ to $P_{Q_2}=0$ and, consequently, $M_{kQ_1} < 1$ to $M_{kQ_2}=1$.

The effect of $\delta\phi$ on the perpendicular velocity of an ion-particle crossing the boundary Q_1 is given by

$$v_{npQ_2}^2(\delta\phi) = v_{npQ_1}^2 + 2Z_p e\,\delta\phi/m_i. \tag{21}$$

Then, the implicit equation for determining $\delta\phi$ is

$$P(\delta\phi) = \frac{1}{k\Delta t \Delta A} \sum_k \sum_p \frac{N_p Z_p}{v_{npQ_2}} \left(\frac{1}{T_e} - \frac{Z_p}{m_i v_{npQ_2}^2} \right) = 0. \quad (22)$$

Solving of Eq. (22) is cumbersome because it involves the velocities of (tens of) particles crossing the boundary node in k timesteps (in fact, this detailed information is not stored in our computer implementation). Based on the ansatz $e\delta\phi \ll T_e$ condition, Eq. (22) is exchanged by its linear approximation

$$P(0) - \delta\phi \frac{dP}{d\delta\phi}(0) = 0, \quad (23)$$

the minus sign coming from the definition of $\delta\phi$ in Eq. (10). Then, calling

$$P_j(\delta\phi) = \frac{1}{k\Delta t \Delta A} \sum_k \sum_p \frac{N_p Z_p^j}{m_i^{j-1} v_{npQ}^{2j-1}(\delta\phi)}, \quad j = 1,2,3, \quad (24)$$

and taking into account that

$$P = T_e^{-1} P_1 - P_2, \quad dP_j/d(\delta\phi) = (1-2j) e P_{j+1},$$

Eq. (23) yields

$$e\delta\phi = \min\left\{ \frac{P_2(0)T_e - P_1(0)}{3P_3(0)T_e - P_2(0)}, e\delta\phi_{\max} \right\}, \quad (25)$$

with $e\delta\phi_{\max}$ a safety limit again. The plasma density in the BC forcing layer decreases from $n_{eQ_1} = P_1(0)$ to

$$n_{eQ_2} \simeq n_{eQ_1} - e\delta\phi P_2(0). \quad (26)$$

The Mach–Bohm numbers at the layer edges, obtained from the linearized equation Eq. (23), satisfy

$$M_{kQ_1}^2 = \frac{P_1(0)}{T_e P_2(0)}, \quad M_{kQ_2}^2 = \frac{1}{T_e} \frac{P_1(0) - (e\delta\phi)P_2(0)}{P_2(0) - 3(e\delta\phi)P_3(0)},$$

with $M_{kQ_2} = 1$ if $\delta\phi_{\max}$ is not used in Eq. (25).

Figures 6(a) and 6(b) show $M_{k,Q_2}(t)$ and $n_e(t)$ at the control node after using the KBF in addition to the ESW. These figures are to be compared with Figs. 5(c) and 5(d). Figure 6(a) illustrates the effectiveness of the KBF algorithm: $M_{k,Q_2} \geq 1$ almost always; instants with $M_{k,Q_2} < 1$ are due to $\delta\phi_{\max}$ and have no impact on the average response. Figure 6(b) shows a decrease on the transit-time oscillation amplitude of $n_e(t)$ with respect to Fig. 5(d), with the same k. This makes unclear whether that reduction is physical or an averaging effect caused by a too high value of k. In any case, a criterion to select an optimal k seems advisable. This criterion would trade-off between a low numerical noise and a minimum alteration of physical effects. Figure 6(c) plots the distribution functions of single and double ions at point Q_1. The average perpendicular energies for single and double ions are 5.8 and 13.2 eV, respectively, and the average T_e is 10 eV, values that agree well with simple estimates.

Figure 7(a) shows time-averaged values of the Mach–Bohm number along the outer wall without and with application of the KBF; in this last case values at both Q_1 and Q_2 are shown. The self-sustaining effect of the BC forcing algorithm, already noticed by Lampe *et al.*, is evident here: the KBF increases the time-averaged Mach–Bohm number at the

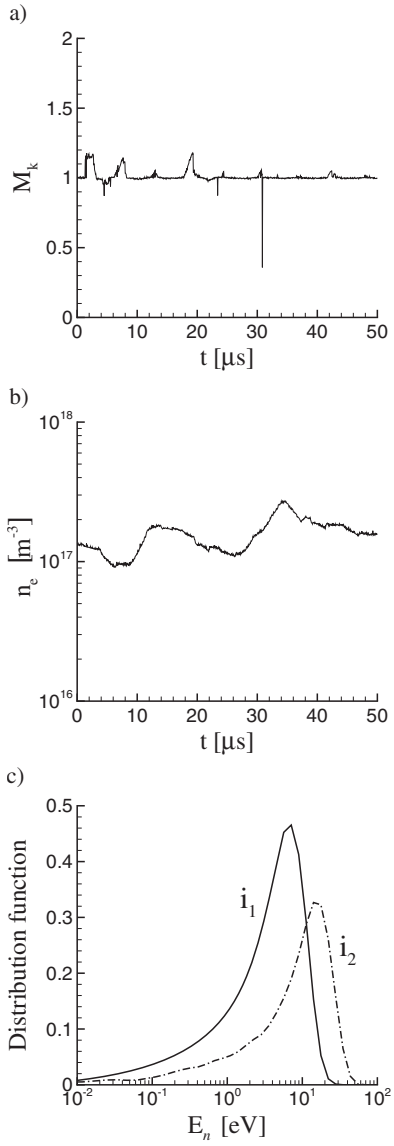

FIG. 6. Effect of applying the KBF to the ESW with $k=50$ at the control node. [(a) and (b)] Instant values of the Mach–Bohm number and the plasma density. (c) Normalized distribution functions of single and double ions vs the particle perpendicular energy E_n; $n_{i_2}/n_{i_1} \simeq 1.4\%$. Results are for simulation 2.

boundary of the PIC domain from $M_k \sim 0.5$ (without KBF) to $M_{k,Q_1} \sim 0.9$. The time-averaged potential fall to achieve $M_{k,Q_2} = 1$ is plotted in Fig. 7(b) together with its temporal dispersion. That potential turns out to be very small inside the chamber ($e\delta\phi/T_e \sim 10^{-3} - 10^{-2}$) and small in the plume ($e\delta\phi/T_e \sim 10^{-1}$). Notice that $e\delta\phi$ is indeed marginal compared to the sheath potential fall, which is one to five times T_e.[13] Since $T_e/2$ is also a measure of the typical perpendicular energy of ions when reaching the sheath edge, $e\delta\phi/T_e \ll 1$ implies that only ion particles with very low perpendicular energy, say with $E_n \leq O(e\delta\phi)$ are affected by the KBF. This agrees perfectly with the fact that the fulfillment of the kinetic BC is very sensitive to particles with a low v_n [Eq. (15)]. A shift by $e\delta\phi$ of the distribution functions at Q_1, plotted in Fig. 6(c), yields an approximate image of the dis-

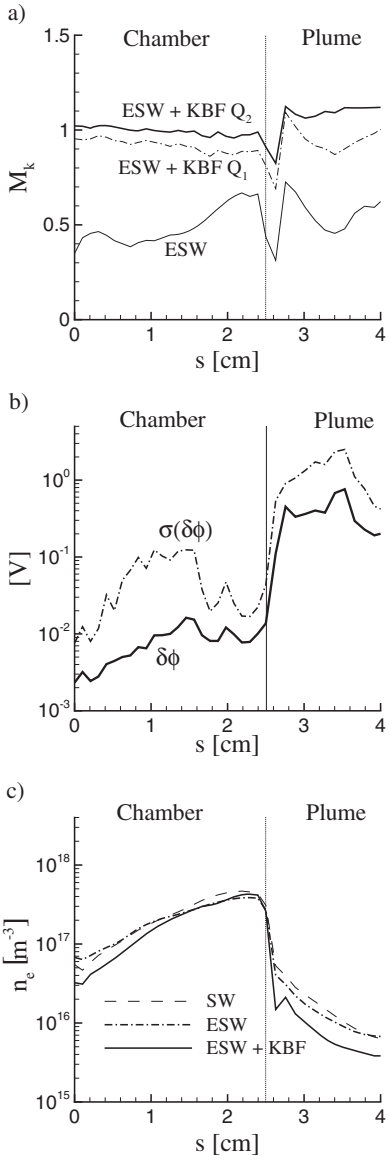

FIG. 7. Time-averaged values along the outer wall for the ESW+KBF, $k=50$, and simulation 2. (a) Mach–Bohm numbers at Q when only the ESW is applied, and at Q_1 and Q_2 when the KBF is supplemented. (b) Potential fall at the BC forcing layer and its temporal standard deviation. (c) Plasma density for different weighting schemes.

tribution functions at Q_2. Since Fig. 6(c) is logarithmic on E_n, only the small-velocity tail of the distributions notice the shift.

Finally, Fig. 7(c)—that complements Figs. 2(c) and 2(d)—illustrates the effect of the ESW and the KBF on the time-averaged plasma density along the outer wall. The change from SW to ESW reduces the large numerical noise near the sheath boundary but has little impact on the time-averaged plasma density and other plasma magnitudes. The change from ESW to ESW+KBF reduces n_e by a factor of about 2 in the regions with large ion velocity dispersion (the upstream and downstream ends of the simulation domain).

V. FINAL CONSIDERATIONS

A. Influence of electrons and walls

The fulfillment of the BC concerns mainly the ion distribution function. The details of (a) the distribution function of confined electrons and (b) the electron-wall interaction have a minor role. In the kinetic BC (13), the electron influence is reduced to set the effective temperature in Eq. (11). [A different case, uncommon and not treated here, corresponds to positive sheaths when electrons are not confined. Then the general BC (9) does not lead to Eq. (10). A particular application of this situation was studied in Ref. 27.]

With respect to the electron-wall interaction, up to here, we have been concerned only with dielectric walls (the lateral walls of a Hall thruster chamber). Nonetheless, that study already covers different electron-wall interaction behaviors, depending on the local SEE yield, which ranges from almost 100% where T_e is high (and the Debye sheath is charge-saturated) to a modest value near the anode.[13] Relative energy losses increase by almost two orders of magnitude from zero SEE to the sheath charge-saturated regime.[28] In spite of this, the values of M_k along the outer wall in Fig. 5(a) indicate that the wall SEE has no influence on the fulfillment of the BC.

In order to further confirm the little effect of electrons and walls on the BC issue, Figs. 8(a)–8(c) show results for the anode wall. The anode differs from the dielectric walls in three aspects: (1) it is a metallic, current-driving wall, (2) there is no significant SEE, and (3) the incidence of the magnetic field, which governs largely the electron motion, is very different, as observed in Fig. 1(b). The comparison of Figs. 8(a)–8(c) with, respectively, Figs. 5(a), 7(a), and 7(c), indicates that the trends and conclusions for the dielectric walls applied to the anode. Observe, in particular, the self-adjustment of M_k at Q_1 from about 0.4 to 0.95 when the KBF is applied.

B. On the "supersonic" Bohm criterion

The BC forcing algorithm of Lampe *et al.* imposes the restrictive or "sonic" form of the BC, $M_0=1$, whereas ours applies the general form, $M_k \geq 1$ (or $M_0 \geq 1$ for a near monoenergetic population). There are two reasons of consistency for our decision. First, since the sheath solution requires only $M_k \geq 1$, the imposition of $M_k=1$ must be supported by arguments that assure that $M_k \leq 1$ always in the bulk plasma. These arguments are not found in discharges with relatively large temporal oscillations of physical nature (which is usually the case of transit-time and breathing oscillations[29] in the Hall thruster discharge). If those oscillations exist, setting the restrictive criterion $M_k=1$ would mean an invasive action on the plasma response. If plasma oscillations are not too large, we expect our algorithm to fulfill $M_k \simeq 1$ by its own, which is the case of M_k in Fig. 6(a) in most instants. Solutions with $M_k > 1$ caused by a physical temporal oscillation are shown in Fig. 9(a), which corresponds to a simulation with a 600 V discharge, where transit-time oscillations are higher, as T_e in Fig. 9(b) shows. Observe the bumps with $M_k > 1$ lasting of the order of a transit-

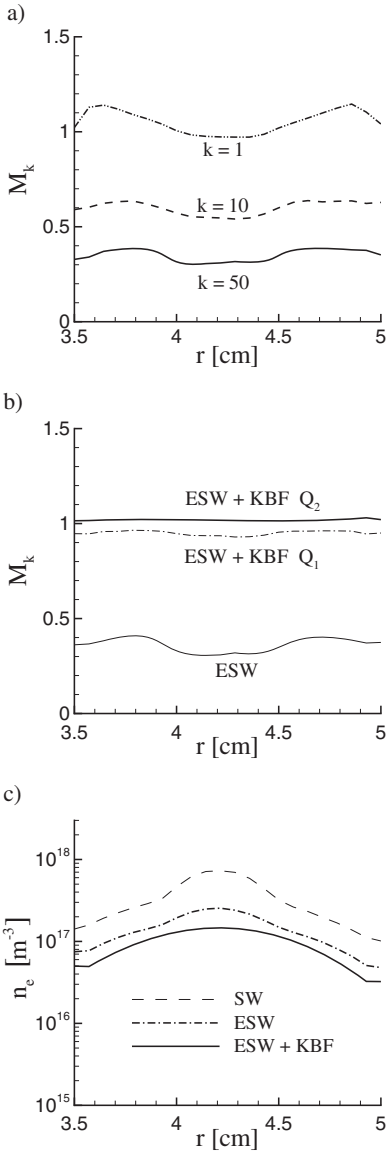

FIG. 8. Time-averaged values along the anode when the ESW with $k=50$ is applied to simulation 2. Plots (a), (b), and (c) correspond, respectively, to the same cases than Figs. 5(a), 7(a), and 7(c).

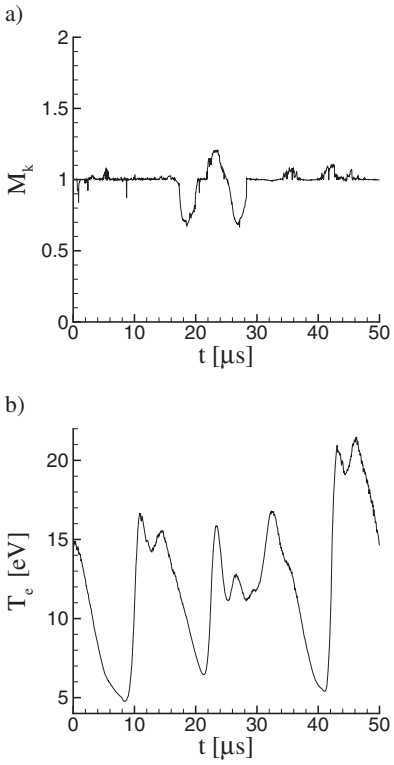

FIG. 9. Instants values at the control node of the Mach–Bohm number and the electron temperature for a simulation with a discharge voltage of 600 V. The ESW($k=50$)+KBF scheme is applied.

time half-period, which must be considered the physical response to plasma oscillations. [The two wells with $M_k < 1$ have a physical origin too but they are not physical themselves, just the effect of applying $\delta\phi_{\max}$.] The second reason for the KBF algorithm to allow $M_k > 1$ is that imposing $M_k=1$ implies a BC forcing layer with $\phi_{Q_2} > \phi_{Q_1}$, which *cannot* be matched to the electric fields in the Debye sheath and the bulk of the plasma, which have a reverse sign.

C. Summary and conclusions

The transition between a quasisteady, negative sheath and a time-dependent quasineutral plasma requires the fulfillment, at the sheath edge, of the BC in its general inequality form. Ion velocity distribution functions in PIC models (and real devices) present a large dispersion, which augments when ions of different charge numbers are present. For these distributions, the widely used, simple expression of the BC, based on a monoenergetic ion population can underestimate significantly the exact, kinetic BC. A Mach–Bohm number M_k, not based on a fluid velocity, is proposed as the suitable variable for measuring the fulfillment of the kinetic BC.

The evaluation of plasma magnitudes at the domain boundaries of a quasineutral PIC model requires a reliable boundary weighting scheme. It is shown, first, a direct relation between the BC fulfillment and the development of wall-perpendicular gradients in the quasineutral plasma. Second, the standard VW used in internal nodes needs a correction when applied in a boundary node. Third, as an alternative, we propose a SW scheme, of similar computational cost and better results in terms of BC fulfillment. Fourth, in order to reduce the numerical oscillations of the SW scheme this must use a time interval one order of magnitude larger than the typical one for the VW at internal nodes.

For practical PIC meshes and in order to reproduce the nonlinear behavior of the plasma potential around the sheath edge and satisfy the kinetic BC, the ESW must be supplemented by a kinetic BC forcing algorithm. The KBF postulates the presence of a thin, collisionless, quasineutral, BC-forcing layer with the incremental potential fall necessary to accelerate the ion flux to $M_k=1$ at the sheath edge. Because of the large sensitivity of the kinetic BC to particles with small perpendicular velocities and the self-adjusting character of the scheme, the incremental potential fall is very small. Our BC-forcing algorithm is shown to be more consistent than the original one by Lampe *et al.* in two central aspects: it is energy-conserving and based on the kinetic BC instead

of the simple BC. In addition, our BC-forcing algorithm applies the general form, $M_k \geq 1$, instead of the restrictive form, $M_k = 1$.

Finally, this study has attempted to demonstrate that the ESW combined with the KBF is an effective and reliable boundary weighting scheme for PIC models of ions. Its reliability is based on the continuous and convergent trends observed in the comparison of different weighting schemes. Furthermore, since we have shown that confined electrons and wall types have little influence on the BC, the conclusions here are expected to be of application to an ion PIC model with different electron formulations.

ACKNOWLEDGMENTS

This work was supported by the Gobierno de España (Plan Nacional de I+D+i, Project No. ESP2007-62694). F.I.P. would like to thank EPSRC-GB and Christ Church at University of Oxford for their support.

[1] L. Tonks and I. Langmuir, Phys. Rev. **34**, 876 (1929).
[2] D. Bohm, *The Characteristics of Electrical Discharges in Magnetic Fields* (McGraw-Hill, New York, 1949), p. 77.
[3] E. Harrison and W. Thompson, Proc. Phys. Soc. London **74**, 145 (1959).
[4] K. Riemann, J. Phys. D: Appl. Phys. **24**, 493 (1991).
[5] M. A. Raadu, Phys. Rep. **178**, 25 (1989).
[6] E. Ahedo, J. Sanmartín, and M. Martínez-Sánchez, Phys. Fluids B **4**, 3847 (1992).
[7] E. Ahedo and M. Martínez-Sánchez, Phys. Rev. Lett. **103**, 135002 (2009).
[8] C. Birdsall and A. Langdon, *Plasma Physics via Computer Simulation* (IOP, Bristol, 1991).
[9] I. Hutchinson, Plasma Phys. Controlled Fusion **44**, 1953 (2002).
[10] M. Lampe, G. Joyce, W. Manheimer, and S. Slinker, IEEE Trans. Plasma Sci. **26**, 1592 (1998).
[11] J. Fife and M. Martinez-Sanchez, AIAA Paper No. 96-3197, 1996.
[12] J. M. Fife, "Hybrid-PIC modeling and electrostatic probe survey of Hall thrusters," Ph.D. thesis, Massachusetts Institute of Technology, 1998.
[13] F. Parra, E. Ahedo, M. Fife, and M. Martínez-Sánchez, J. Appl. Phys. **100**, 023304 (2006).
[14] F. Parra, D. Escobar, and E. Ahedo, AIAA Paper No. 2006-4830, 2006.
[15] I. Maqueda, D. Escobar, and E. Ahedo, *30th International Electric Propulsion Conference*, Florence, Italy (Electric Rocket Propulsion Society, Fairview Park, OH, 2007), Paper No. IEPC 2007-066.
[16] D. Escobar and E. Ahedo, IEEE Trans. Plasma Sci. **36**, 2043 (2008).
[17] G. Hagelaar, J. Bareilles, L. Garrigues, and J. Boeuf, J. Appl. Phys. **91**, 5592 (2002).
[18] M. K. Scharfe, N. Gascon, M. A. Cappelli, and E. Fernandez, Phys. Plasmas **13**, 083505 (2006).
[19] J. Koo and I. Boyd, Phys. Plasmas **13**, 033501 (2006).
[20] F. Parra, E. Ahedo, M. Martínez-Sánchez, and J. Fife, *SP-555: 4th Spacecraft Propulsion Conference*, Sardinia, Italy (European Space Agency, Noordwijk, The Netherlands, 2004).
[21] F. Parra and E. Ahedo, AIAA Paper No. 2004-3955, 2004.
[22] D. Escobar, E. Ahedo, and F. I. Parra, *Proceedings of the 29th International Electric Propulsion Conference*, Princeton (Electric Rocket Propulsion Society, Fairview Park, OH, 2005), Paper No. IEPC-2005-041.
[23] F. Parra, Actualización y mejora de un código PIC-fluido bidimensional para el flujo de plasma en motores de efecto Hall, Engineer Degree Thesis (available at http://web.fmetsia.upm.es/ep2/), Universidad Politécnica de Madrid, 2004.
[24] S. Barral, K. Makowski, Z. Peradzynski, and M. Dudeck, Phys. Plasmas **12**, 073504 (2005).
[25] K. Riemann, IEEE Trans. Plasma Sci. **23**, 709 (1995).
[26] R. Santos and E. Ahedo, AIAA Paper No. 2009-4913, 2009.
[27] E. Ahedo and D. Escobar, Phys. Plasmas **15**, 033504 (2008).
[28] E. Ahedo, Phys. Plasmas **9**, 4340 (2002).
[29] S. Barral and E. Ahedo, Phys. Rev. E **79**, 046401 (2009).